Chapter 12
Cryo-Electron Microscopy and Cryo-Electron Tomography of Viruses

Daniel Luque and José R. Castón

Abstract When viruses are viewed as dynamic containers of an infectious genome, their structural, physical, and biochemical analyses become necessary to understand the molecular mechanisms that control their successful life cycle. Information on virus structures at the highest possible resolution is essential for identifying the principles of their structure–function relationship, and could lead to development of antivirals, vaccines, and the advancement of new platforms for virus-based nanotechnology. Cryogenic electron microscopy (cryo-EM), which has revolutionized structural biology, is central to determining high-resolution structures of many viral assemblies, within a feasible time frame and in near-native conditions. In addition, cryo-EM allows dynamic studies of functional complexes that are often flexible or transient. State-of-the-art approaches in structural virology now extend beyond purified symmetric capsids and focus on the asymmetric components such as the packaged genome and minor structural proteins that were previously missed. A variation of cryo-EM, cryo-electron tomography (cryo-ET), can handle pleomorphic and complex viruses as well as viruses in the cellular context at unprecedented resolution. These and other emerging methods will support studies to address viral entry, assembly, replication and egress within the cellular host. This review describes the use of cryo-EM and cryo-ET in structural virology, and provides a few recent examples of how these techniques have been applied successfully in basic research to decipher fundamental aspects of virus biology and to investigate threatening viruses, including SARS-CoV-2, responsible for the COVID-19 pandemic.

Keywords Capsid · Cryo-electron microscopy · Cryo-electron tomography · Three-dimensional reconstruction · Viral assemblies · Virus life cycle

D. Luque
Spanish National Microbiology Centre, Institute of Health Carlos III, Madrid, Spain

J. R. Castón (✉)
Department of Structure of Macromolecules, Centro Nacional de Biotecnología (CNB-CSIC), Campus Cantoblanco, Madrid, Spain
e-mail: jrcaston@cnb.csic.es

Nanobiotechnology Associated Unit CNB-CSIC-IMDEA, Campus de Cantoblanco, Madrid, Spain

M. Comas-Garcia and S. Rosales-Mendoza (eds.), *Physical Virology*, Springer Series in Biophysics 24, https://doi.org/10.1007/978-3-031-36815-8_12

Introduction

To understand the principles of the structure, function, and evolutionary relationships of virus and viral macromolecular assemblies, structural information at the highest possible resolution is essential. This analysis can also lead to the development and design of antiviral drugs and vaccines [1], and to advancement of new platforms for virus-based nanotechnology [2]. The three major techniques in current use for structural determination are X-ray crystallography, nuclear magnetic resonance (NMR) spectroscopy, and cryogenic electron microscopy (cryo-EM). Three-dimensional (3D) cryo-EM provides an effective means of determining the structure of many macromolecular assemblies at atomic or near-atomic resolution [3, 4], as highlighted by the 2017 Nobel Prize in Chemistry, awarded in recognition of the extraordinary impact of cryo-EM on many scientific disciplines [5].

For 3D cryo-EM, rapid freezing immobilizes a radiation-sensitive sample in vitreous ice (water molecules in an amorphous state) in a near-physiological environment, and protects it from radiation damage during imaging. A unique application of vitrification is its ability to capture complexes in their multiple native states and trap intermediates at fixed time points (also termed time-resolved cryo-EM). Whereas X-ray crystallography is limited by the difficulty of crystallizing large, flexible complexes, as well as by the large quantities of material needed for crystallization trials, NMR is limited by the size of the macromolecules under study. In structural biology, 3D cryo-EM is currently a go-to technique for three main reasons, (i) the broad molecular weight range available for study (~50–100,000 kDa), (ii) the need for a (relatively) small amount of sample, and (iii) the ability to deal with heterogeneous samples to discern multiple conformational (or compositional) states [6–8].

3D cryo-EM can be used to study samples from single proteins [9, 10] to large macromolecular complexes such as virus particles [7, 8]. Cell organelles, entire eukaryotic cells, bacteria, and tissue sections can be analyzed by an analogous method known as cryogenic electron tomography [11, 12] (cryo-ET). In virology, it also enables rapid structural analysis of emerging viruses [13]; for example, cryo-EM was pivotal in combating several viruses implicated in recent deadly epidemics, such as Ebola (2014–2016) [14], Zika (2015–2016) [13], dengue (2019–2020) [15], MERS-CoV (2012–2015) [16, 17], and recently, SARS-CoV-2.

Owing to their large mass and high symmetry, viruses and viral assemblies were (and are) a major driving force in cryo-EM development. Cryo-EM includes several imaging modes through a transmission electron microscope (TEM); single-particle analysis (SPA) and electron cryo-tomography (cryo-ET) are the methods most extensively used, as they can address a wide range of biological problems. SPA is ideal for structure determination at near-atomic resolution of infectious virions of a broad size range, viral macromolecular assemblies that are large and dynamic, with compositional heterogeneity (states that present intermediate functional conformations during assembly), soluble proteins such as viral polymerases or surface spikes, and the

genome that follows an asymmetric organization. The structure of apoferritin, a 24-subunit protein nanocage (similar to a closed icosahedral capsid) was recently solved at 1.2 Å resolution using SPA cryo-EM, and individual hydrogen atoms in the protein were clearly located [18, 19]. Cryo-ET enables analysis at unprecedented resolution of non-symmetric, pleomorphic, and/or complex viruses, and of viruses not only in their native physiological state, but also in their natural cell environment (in situ). Sub-volume or sub-tomogram averaging [STA, averaging of repeating structures from tomographic reconstructions, or tomograms [20] can be further exploited to resolve higher resolution detail of any repeating structures such as the viral surface glycoproteins of SARS-CoV-2 [21] and the internal HIV nucleocapsid [22].

Here we describe the basis of the cryo-EM and cryo-ET to the study of viruses, discuss some recent examples and approaches that highlight the strength of cryo-EM, and describe how SPA and cryo-ET are revolutionizing our understanding of virology across the resolution scale, from cells to atoms. The development of direct electron detectors (DED) for recording images was a key factor driving the "resolution revolution" [23, 24], in addition to improvements in preparation methods, the development of dedicated cryo-electron microscopes, and computational methods to deal with structural/compositional heterogeneity [25]. As a result, many challenging topics in virology previously unsuitable for cryo-EM analysis, such as packaged viral genome structure, jumbo viruses, heterogeneous viruses, or high-dynamic viral surface assemblies, can now be determined feasibly, many at near-atomic resolution (2–4 Å). Finally, we briefly describe recent advances in visualizing the virus life cycle in situ using cryo-ET.

Sample Preparation and Grids

Specimens are initially examined by negative staining, in which samples are dehydrated and embedded in a heavy metal salt cast that replicates specimen shape [26]. This quick, simple method is used to assess sample homogeneity and quality, as it provides high-contrast images.

For cryo-EM, the sample is immobilized in a thin film of vitreous (amorphous) ice that prevents structural alterations in the specimen caused by ice crystal formation [27]. To prepare these vitrified samples, an aliquot (~3 μL) of the specimen in its buffer is applied to an electron microscopy grid coated with a holey carbon support film (for example, Cu/Rh Quantifoil grids). It is then blotted with filter paper to yield a very thin film of the particle suspension in the holes. The grid is then plunged into liquid ethane cooled by liquid nitrogen [28, 29]. Vitreous ice will ideally be uniform across the entire grid, only slightly thicker than the assembly/molecule of interest, and will contain well-distributed particles at sufficient concentration. To improve reproducibility, this is done using robotic plunge-freezer devices such as a Vitrobot (Thermo Fisher Scientific, TFS), Cryo-plunge (Gatan), or EM GP2 (Leica

Microsystems). At −180 ºC, vitrified ice does not sublimate significantly in the high-vacuum conditions of the electron microscope column, and protects the sample from radiation damage [30–32].

In recent years, it was shown that that macromolecules under study can interact preferentially with the air–water interface (AWI) and/or can (fully or partially) denature on exposure to it. Vitrification by formation of a thin solvent film using blotting paper followed by plunging into cryogens usually takes some seconds in which the sample could contact AWI [33, 34]. Different approaches are being developed to improve cryo-EM sample quality and reproducibility, including (i) direct sample deposit onto self-wicking grids using an inkjet piezo dispenser (Spotion/Chameleon) [35], (ii) using microcapillarity for sample deposit (cryoWriter) [36], (iii) spraying sample onto the grid with an ultrasonic humidifier [37], (iv) pin printing followed by vitrification with a cryogen stream (Vitrojet) [38], and (v) time-resolved by microfluidic spraying (TED) [39].

The buffered sample concentration is critical for obtaining a thin film with uniform specimen distribution after blotting (confirmed by negative staining analysis). When sample concentration is limited, a continuous carbon support foil is used rather than the holey film. UltrAuFoil grids (holey gold support foil on gold grids) provide another alternative. The presence of sucrose or cesium chloride, used in sample purification by cushion and density gradient ultracentrifugation, reduce vitrification efficiency, as does the glycerol used to preserve frozen samples. These compounds bubble when exposed to the electron beam and are therefore incompatible with high-resolution imaging [25]. When carried out correctly, this method provides a near-physiological, water-like environment for the specimen, leaving the native structure preserved.

Sample stability and homogeneity should be checked by conventional biochemical and biophysical analyses prior to cryo-EM analysis [40]. Size exclusion chromatography separates specimen subpopulations based on the hydrodynamic radius of their particles, and is an appropriate method for preparing homogeneous samples [41, 42]. In addition to contaminant complexes, specimen heterogeneity can result from a sample in distinct compositional or conformational states. The GraFix technique can also be used to help ‘purify’ the sample [43]; here, a chemical crosslinker (e.g., glutaraldehyde) is used to stabilize complexes from dissociated elements and aggregations.

Image Acquisition

The major factor that limits resolution of the cryo-EM structure is radiation damage caused by energy deposition from electron beams to the sample. Use low electron doses to prevent radiation damage nonetheless leads to noisy low-contrast images with a very poor signal-to-noise ratio (SNR) for subsequent image processing, for

example hindering the accuracy of particle alignment and atomic-resolution reconstruction. Hence many different views of the same macromolecular complex are averaged to enhance the SNR and calculate a 3D reconstruction.

DED, such as the Falcon camera (from FEI Thermo Fisher), the K camera (Gatan), and the DE camera (Direct Electron Inc.) became pivotal in achieving improved achievable resolution. DED are complementary metal oxide semiconductor (CMOS)-based sensors that convert electrons directly into an electrical current with high detective quantum efficiency (DQE), a measure of detection efficiency as a function of spatial frequency [44, 45] that increases the SNR. DED can operate in integration or counting mode. In integration mode, the signal is either integrated over the entire exposure time or dose-fractionated into multiple movie frames. In counting mode, single electron scattering events are detected. Although integrative mode was faster and counting optimized the acquisition quality, more recent detectors (like Gatan K3 and TFS Falcon 4) are able to record high quality counting acquisitions at high speed (up to 900 exposures/hour).

DED have high frame-rate acquisition and images are collected as movies or a collection of frames; this allows dose fractionation into multiple frames per second [46, 47] (each frame has an extremely low electron dose, 0.5-1e^{-}/pixel). More importantly, the beam-induced movement of the specimen and support foil (and/or the mechanical drift of the stage) that results in motion-induced image blurring can be tracked and corrected by computational alignment of a series of low-dose frames taken in one area before averaging [48] (Fig. 12.1). Subframes with optimized doses can also be selected for subsequent image processing [49] (later frames would be of lower quality due to radiation damage). The combination of dose fractionation and motion correction greatly improves data acquisition efficiency—nearly all images are of a quality suitable for recovering high resolution information [50]. Beam-induced motion is greatly reduced by using holey gold support foil [51] (for example, UltrAuFoil grids). HexAuFoil grids (hexagonal-pattern gold grids of gold foil with $< 0.3\ \mu m$ holes) [52] almost eliminate beam-induced motion during imaging.

Because of the large depth of field in the electron microscope, each micrograph is a projection through the specimen, yielding 2D information. These 2D projection images are modulated by the contrast transfer function (CTF) of the microscope, and image defocus correction is required for accurate interpretation of specimen structure. The CTF is a characteristic function of each microscope (the spherical aberration coefficient of the objective lens, Cs) and the imaging settings (defocus level, beam coherence, and accelerating voltage). By choosing different defocus settings, specific image frequencies can be accentuated at the expense of others. In appropriate conditions, a contrast-enhancing effect can thus be obtained. CTF-modulated information implies the existence of frequency ranges in which there are no data (zeros in the CTF), as well as frequency regions in which the information has reversed contrast (between the first and the second zero, between the third and fourth zero, and so on). It also considers the attenuation of useful information at higher frequencies, the so-called envelope function, which is dependent mainly on the beam coherence.

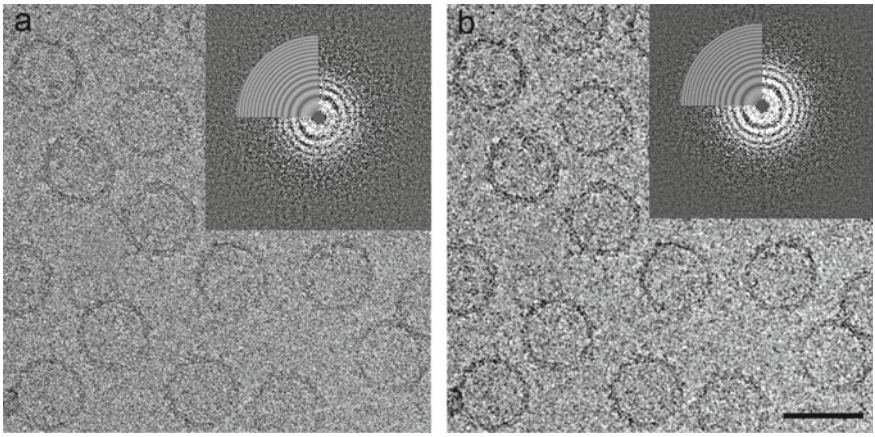

Fig. 12.1 Correction of beam-induced motion and recovery of high-resolution information. **a** Uncorrected two-dimensional movie average. **b** Two-dimensional movie average after translational alignment. Cryo-EM image corresponds to vitrified empty capsids of Rosellinia necatrix quadrivirus 1, a ~450-Å-diameter, fungal virus. Barr = 500 Å. Power spectra calculated from the averaged movie before (**a**) and after (**b**) motion correction are shown. Motion correction restores Thon rings from ~6–7 (**a**) till 3–4 Å (**b**) resolution. The top left corner of each power spectrum shows a CTF model fit to the experimental Thon rings

During data acquisition, images are recorded at a range of defocus settings to enhance different features of the specimen and to fill in missing information when they are combined into a 3D reconstruction. Averaged movie quality can be analyzed by inspection of the CTF zeros or Thon rings in the images' computed diffraction patterns. Large symmetrical assemblies (such as viruses) are relatively easy for a computer to motion-correct and can be imaged at small defocus levels with good image contrast and preserved high-resolution signals. For small (100–300 kDa) and asymmetric assemblies, higher defocus settings are needed, which limit the resolution that can be achieved.

A number of automated data collection software packages such as free SerialEM [53] and Leginon [54], as well as the commercial EPU (TFS), JADAS (JEOL) [55], and Latitude S (Gatan) systems are available for collecting large data sets for reliable statistical analysis.

Structure Determination by SPA

The general SPA workflow involves quality assessment of motion-corrected average images, particle picking (arduous with low molecular weight specimens), image defocus estimation and CTF correction, 2D particle classification and alignment, estimation of particle orientation and refinement, image reconstruction and 3D refinement, resolution assessment, and cryo-EM map validation [56] (Fig. 12.2).

Projection subtraction and local reconstruction are used routinely to deal with non-symmetric or flexible components of the complex analyzed (below). A number of image processing packages can perform these tasks, provide improved classification of multiple conformational or compositional states, and sort images into different 2D and 3D image classes. All this has become computationally feasible with improved central processing units (CPU) and, more recently, graphic processing units (GPU). These software packages include RELION [57], EMAN2 [58], cryoSPARC [59] and FREALIGN [60]. SCIPION [61] provides a framework for integrating software packages via a workflow-based procedure designed for less experienced users, and offers user-friendly graphic interfaces. Most macromolecular complexes are intrinsically dynamic and normally contain many different conformational (or compositional) states. This structural heterogeneity becomes the major limiting factor for attainable resolution in cryo-EM. Additional methods such as 3D-classification of particle conformations [62–64], non-homogeneous refinement, multibody refinement, refinement of subparticle orientations, per-particle focus and motion refinement, and correction of Ewald sphere effects for large viruses have recently been applied to overcome limitations in the conventional data processing pipeline [65, 66].

SPA provides the 3D structure of examined specimens by computationally merging images of many (easily exceeding tens or hundreds of thousands) individual macromolecules of a homogeneous subset that have been aligned with one another at high precision. Each particle image is a randomly orientated 2D projection image that contains all the structural detail of the 3D specimen. Angular orientation parameters are determined by comparing the 2D projections with spatially defined reprojections of an initial 3D model filtered at low resolution. A new 3D map of the macromolecular complex is then calculated from these 2D projections by "back-projection", that is, the combination of all views into a single 3D map [67]. This projection-matching process is performed iteratively to obtain new 3D reconstructions with improved resolution until no further improvement is possible.

Resolution Estimation, Model Building and Validation

When generating a cryo-EM map, a standard approach is to split the data randomly into two independent sets at the beginning of the data processing procedure and then compute, by iterative refinements and reconstructions, two independent reconstructions from each half-set. These two reconstructions are then correlated as a function of the spatial frequency to determine the extent to which structural features have been reliably reproduced. This is termed the "gold standard" Fourier shell correlation (FSC) method [68, 69]. As the resolution is often non-isotropic in different map regions, a visual inspection of map quality in key regions is needed to establish local conformations and their functional implications [70]. Local variations in resolution

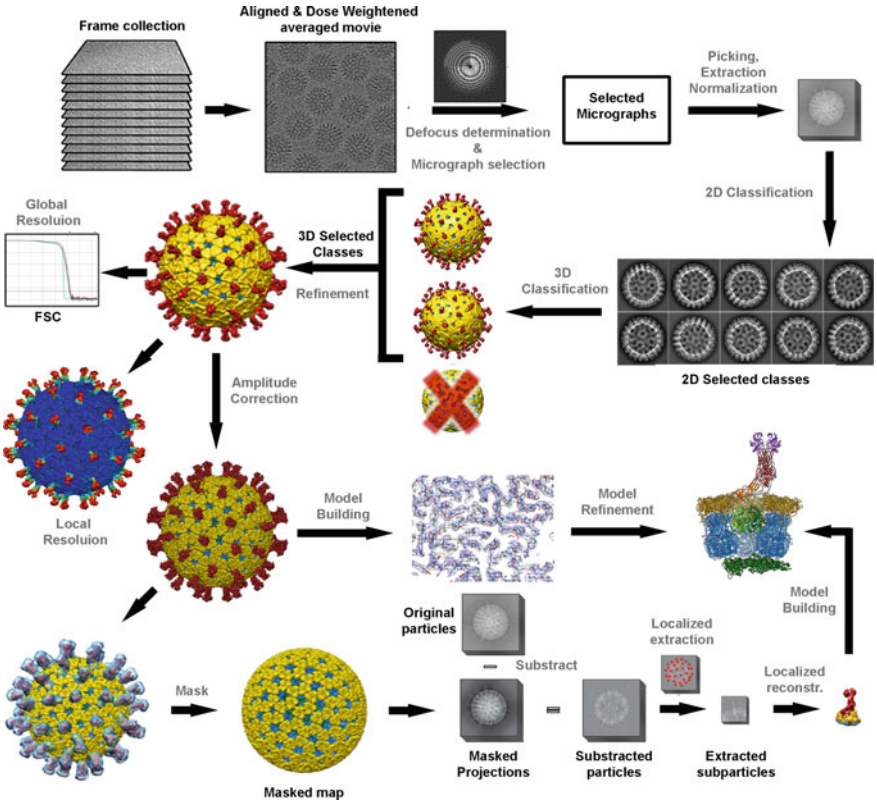

Fig. 12.2 Overview of the single-particle cryo-EM workflow, from data collection to 3D model. The vitrified sample is imaged by collecting movie frames that are aligned, dose weightened and averaged. Using motion-corrected images, image defocus is calculated, good quality micrographs are selected, and individual particles (such as protein cages) are picked. Next, particles are extracted, normalized, and then are subjected to 2D classification and averaging, to get class averages according to their similarity and clean up the data set of bad particles. Selected particles can be used to obtain an ab initio 3D model. This low-resolution model is then used as a reference for 3D classification, a necessary step for identifying distinct conformations, macromolecular heterogeneities or particle subsets with different structural integrity. Orientation refinement is iteratively done until the structure converges, as indicated in the resolution analysis by the FSC method. The final map is amplitude corrected to reveal high-resolution details. Finally, the protein sequence is fitted into the 3D map to build a de novo 3D model of the protein which is refined to obtain a final model. If necessary, particles with the density corresponding to certain regions of the 3D structure subtracted can be obtained by subtracting the projections of the final map after mask the volumes of interest. In order to analyze non symmetric components of the structures, once final orientations has been assigned to each particle, it is also possible to extract subparticles the corresponds to a 3D coordinate (and their symmetry related mates) in the reconstructed map. 2D images and 3D maps correspond to the cryo-EM structure of the rotavirus triple layered particle

can be assessed using Resmap [71] or MonoRes [72] programs. Differences in cryo-EM local resolution values can be taken as a signature of conformational fluctuations at equilibrium in solution [73].

Once a 2–4 Å cryo-EM map has been obtained, the next stage is to build and refine a model. The known protein sequence is fitted into the 3D map by positioning the bulky amino acid side chains first, allowing de novo structure determination. The 3D atomic model built is then subjected to further refinement. Homology models of atomic structures obtained by X-ray crystallography and NMR might also be fitted into a low resolution cryo-EM map (termed the hybrid approach). There are several model-building and validation tools, most of them based on X-ray crystallography analysis, including CCP-EM [74], Phenix [75], Rosetta [76], UCSF Chimera [77], ISOLDE [78], and Coot [79]. Prediction of protein structures from primary sequence information with AlphaFold [80] or RoseTTAFold [81] provide preliminary models that can be built into cryo-EM data.

Cryo-Electron Tomography (Cryo-ET)

Cryo-ET [11, 82] is based on the acquisition of series of projection images collected by tilting the specimen around an axis perpendicular to the electron beam inside the microscope, and combining the resulting "tilt-series" into a 3D volume. The 3D reconstruction of the field of interest, or tomogram, is calculated as a back-projection in real space; assembly of correctly aligned projections is reverse-projected into 3D space. Cryo-ET has allowed the study of samples ranging in size from large (pleomorphic) complexes to organelles, prokaryotic cells, and eukaryotic cell lamellae [thin cell sections obtained by focused ion beam (FIB) milling [83], that is, samples not amenable to SPA averaging method. Similarly to SPA cryo-EM, multiple copies of repeating structures in a tomogram can be extracted as a volume, aligned, and averaged. This STA approach delivers structures of large macromolecular complexes at subnanometer resolution in their native cellular environment [84] and in some cases, by averaging 3D structures instead of 2D images as in cryo-EM, at high resolution [22]. The introduction of correlative light and electron microscopy (CLEM) and focused ion beam (FIB) milling have further empowered cryo-ET to reveal native ultrastructures of large eukaryotic cells or even tissues, with unprecedented spatiotemporal resolution [20, 85].

The structural information within a reconstructed tomogram is limited by three notable factors: low signal in each tilt image to limit accumulated electron dose, missing information due to mechanical limitations in the microscope stage (termed the "missing wedge"), and accuracy of alignments between each successive tilt image prior to reconstructing a 3D volume [11].

Some Recent Major Contributions of Cryo-EM and Cryo-ET in Structural Virology

Due to the ordered nature, structural integrity, and homogeneity of many viral assemblies, cryo-EM is used extensively to solve near-atomic resolution (2–4 Å) structures of infectious virions of a broad size range, with helical or icosahedral symmetry, tailed phages, virus-like particles (VLP), hybrid VLP (with heterologous cargos), and viral complexes that represent intermediate functional states during assembly. Even isolated proteins such as viral polymerases (purified from viruses) or non-structural proteins are analyzed by cryo-EM (cryo-EM ex vivo or ex virio), although these structural targets require much more expertise for cryo-EM sample preparation and optimization. The symmetry-based averaging imposed nevertheless results in the loss of unique (but ubiquitous) asymmetric features. Recent new approaches extend these analyses to the asymmetric organization of the packaged genome and minor structural proteins such as viral polymerases that were previously missed (cryo-EM in situ) [86]. Asymmetric structures have important functions in numerous steps of the virus replication cycle, and many of these might be key targets for the development of new antiviral drugs.

Here we will consider some recent studies showing asymmetric structural features in viruses and the reconstruction methods used to identify these novel or unexpected components associated with essential functions. We will briefly discuss other challenging viral systems such as giant (or jumbo) viruses, and the cryo-EM and cryo-ET contributions in the battle against the COVID-19 pandemic. Finally, we will show the latest structural insights disclosed by cryo-ET into complex and pleomorphic viruses, as well as the mechanisms of its entry, replication, assembly, and budding—all the dynamic steps during the life cycle in the cellular context.

Cryo-EM in situ: Structural Analysis of Asymmetric Components of Icosahedral Viruses

Probing asymmetry in icosahedral and helical viruses can be difficult if the asymmetric feature is small or has a weak signal. An exception is the tailed bacteriophage, with a large assembly that allows correct alignment of the asymmetric assembly. A variety of image processing-based strategies is used to study non-symmetric capsid features; these approaches are (i) standard asymmetric refinement, (ii) symmetry relaxation, (iii) symmetry expansion, and (iv) subparticle classification/refinement [65, 66, 87]. For asymmetric refinement, no symmetry is applied during data processing (C1 symmetry), and orientation sampling is performed on the full orientation space. In the relaxed symmetry approach, the icosahedral orientations determined are relaxed and iterative sampling is tested for the 60 symmetry-related orientations. For expanded symmetry, each of the 60 symmetry-related orientations is assigned to each particle before focused (or masked) classification/

refinement. In subparticle classification and/or refinement, subregions or subvolumes are reextracted and allowed to deviate from icosahedral symmetry.

Analysis of the viral genome is central to understanding dynamic processes of the life cycle such as assembly, infection, and genome replication. Bacteriophage MS2 and Qβ capsids incorporate a single copy of the maturation protein, responsible for binding both viral ssRNA and host receptors and the genome, which is relatively rigid. Asymmetric reconstruction/refinement shows that ssRNA has multiple stem-loops termed packaging signals (PS) that bind cooperatively to a capsid protein recognition motif. The PS act as allosteric switches, control assembly efficiency, and are responsible for in vivo packaging specificity [88, 89]. High resolution asymmetric cryo-EM reconstructions (standard asymmetric refinements) of MS2, which traces 80% of the genome with 16 stem-loops, confirm this assembly model [90–92] (Fig. 12.3a).

Whereas dsDNA viruses in the extracellular life cycle are in a quiescent state, dsRNA virus capsids in the host cytoplasm are dynamic nanocages, and carry out mRNA synthesis using their genome segments as templates for the transcriptional enzyme complexes (TEC; they include an RdRp and other enzymes). In cypovirus, the 10 genomic dsRNA segments have a non-spooled organization and there are 10 TEC anchored to the inner surface of the capsid shell around the five-fold axis, leaving two of the 12 possible positions vacant [93, 96] (Fig. 12.3b). RdRp, resolved to 3.3 Å resolution, are in different conformations in the transcribing and non-transcribing states. These studies relied on subtracting capsid density from the original images, followed either by standard asymmetric refinement [93] or refinement based on relaxing symmetry [96]. Similar in situ structural analyses with rotavirus, reovirus, aquareovirus and bluetongue virus show the mechanism of RNA transcription and replication [97–100]. In bacteriophage ϕ6, with a trisegmented genome, the dsRNA adopts a dsDNA-like single-spooled genome organization and RdRp are detached from the capsid inner surface. These variations might be a consequence of the differences in transcription mechanisms between the two virus families (semi-conservative vs. conservative transcription) [101].

Herpesvirus consists of an inner icosahedral capsid that contains the linear dsDNA genome, a middle proteinaceous tegument layer, and an outer envelope containing transmembrane glycoproteins. The viral genome is packaged/ejected by an ATP-driven terminase through the asymmetric portal complex located at a predetermined fivefold symmetry axis of the capsid. Processing of cryo-EM images of HSV-1 virions using a sequential localized classification and symmetry relaxation allowed decoupling and reconstruction of heterosymmetric and asymmetric capsid elements. The HSV1 map shows the in situ structures of the unique portal vertex, genomic termini, and ordered dsDNA coils [94] (Fig. 12.3c). A similar approach resolved the human cytomegalovirus structures of the portal and the capsid vertex-specific components [102].

Feline calicivirus (FCV) has a positive-sense ssRNA genome encapsidated within a $T = 3$ icosahedral capsid. After binding its receptor, focused classification leads to a portal-like structure formed of 12 copies of VP2 (a minor structural protein) located at a unique threefold symmetry axis [95]. The conformational changes observed in

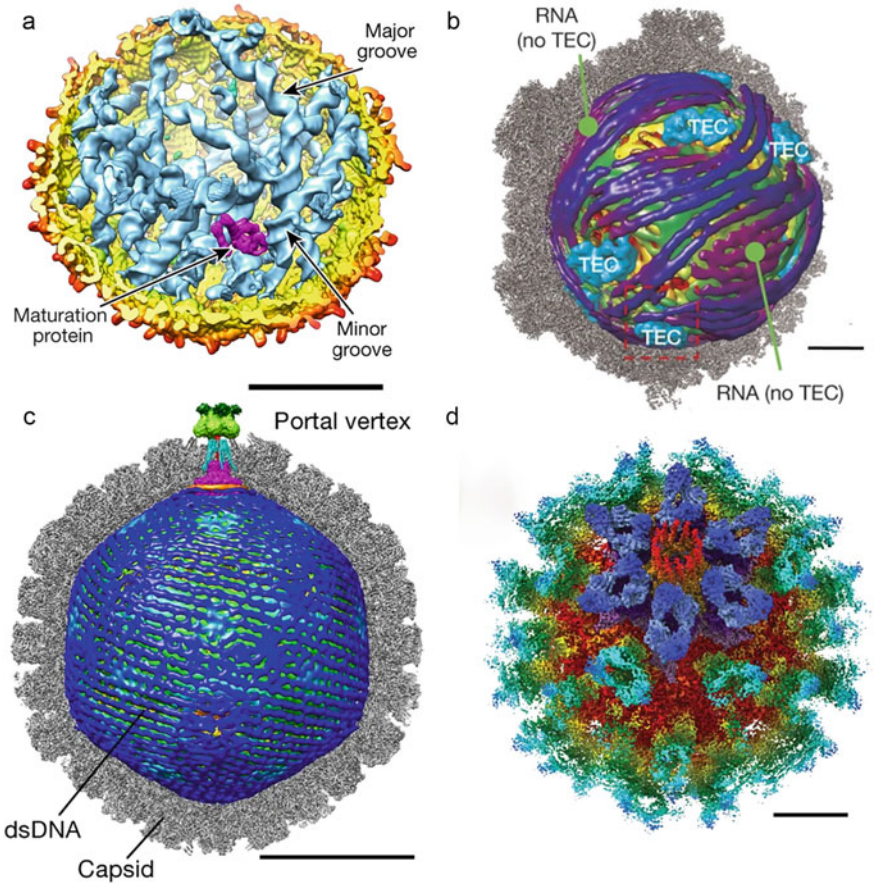

Fig. 12.3 Cryo-EM and asymmetric reconstructions of icosahedral viruses for visualization of the viral genomes and other asymmetric components in situ. **a** A cut-open view of bacteriophage MS2 to show a single copy of the maturation protein (magenta) and the ssRNA viral genome (blue) mostly organized as dsRNA (major and minor grooves of double-stranded regions are indicated). Reproduced with permission from Ref. [90]. **b** Cryo-EM asymmetric reconstruction of cypovirus, with the front half of the icosahedral capsid removed to show the asymmetric components, the dsRNA genome (dark blue) and the transcriptional enzyme complexes (TEC, cyan). Reproduced with permission from Ref. [93]. **c** Herpes simplex virus type 1 (HSV-1) with the front half of the protein shell removed to visualize the portal vertex elements (portal, magenta; portal cap, green) and ordered dsDNA coils (blue) spooled around a disordered dsDNA core. Reproduced with permission from Ref. [94]. **d** Radially colored full feline calicivirus (FCV) virion to highlight the receptor proteins (blue) and the VP2 portal-like assembly (red) at a unique threefold symmetry axis. Reproduced with permission from Ref. [95]. Scale bars 100 Å (a, b and d) and 450 Å (**c**)

the capsid protein VP1 allow for extrusion of the internalized VP2 proteins as well as the formation of a small pore in the capsid shell. The VP2 portal-like assembly might function in a mechanism for endosomal escape and genome delivery, a process not well understood in viruses without membranes (Fig. 12.3d).

Atomic Structures of Jumbo Viruses (>100 nm)

Giant viruses belong to the nucleocytoplasmic large DNA viruses (NCLDV) that include nine families, *Ascoviridae, Asfarviridae, Iridoviridae, Marseilleviridae, Mimiviridae, Pandoraviridae, Phycodnaviridae, Pithoviridae*, and *Poxviridae*, as well as some independent species. These viruses, with the dsDNA genome encapsulated in a lipid bilayer [103], range in size from ~150 nm to 2 μm, and include high-symmetry icosahedral viruses such as Paramecium bursaria chlorella virus 1 (PBCV-1) and amphora-shaped (asymmetric) viruses like Pithovirus.

Two main strategies are applied to calculate high resolution cryo-EM structures of large viruses [104]: (i) use of electron microscopes with high acceleration voltage, e.g., one megavolt cryo high-voltage electron microscopy (1MV cryo-HVEM), which improves sample penetration and overcomes the limitations imposed by electro-optical physics at lower voltages [105], and (ii) the 'block-based reconstruction' method [106].

For thick samples, the influence of depth of field causes an internal focus shift (a focus gradient within a single virus particle), imposing a hard limit on the attainable resolution [107]. Standard CTF correction methods, which assume a single constant defocus for the entire particle, are insufficient for large, high-resolution structures. Increasing the accelerating voltage increases depth of field, however, and improves the (electron) optical conditions in thick samples. For 300 kV electron microscopes, recent advances in image processing, such as Ewald sphere correction to tackle the focus gradient within a single virus particle, can offer great improvements in attainable resolutions. 'Block-based' reconstruction [106] focuses on sub-sections ("blocks") of the virus to allow localized defocus refinement across each particle, and reduces the size of the box required.

For high-resolution 3D SPA of giant viruses, there are currently seven structures that exceed 1 nm resolution: two for PBCV-1 [108, 109], two for African swine fever virus (ASFV) [110, 111], the marseillevirus Singapore grouper iridovirus [112] and Tokyovirus [105]. All were analyzed using 'block-based' reconstruction (with 300 kV microscopes) except Tokyovirus (with a maximum diameter of 250 nm), which was analyzed as a complete viral particle using 1 MV cryo-HVEM. PBCV-1 at 3.5 Å resolution [108] and ASFV at 4.1 Å resolution [111] were solved by cryo-EM SPA. The PBCV-1 and ASFV capsids are composed of one "major" capsid protein (MCP) and a combination of 14 (PBCV-1) or four kinds (ASFV) of "minor" capsid proteins (mCP). The MCP of PBCV-1 and ASFV are trimeric and share the double "jelly roll" motif, each of which consists of eight β strands [113].

SARS-CoV-2 and Viral Spikes

The coronavirus disease 2019 (COVID-19) pandemic, caused by the severe acute respiratory syndrome coronavirus 2 (SARS-CoV-2), is associated with over ~760 million cases and ~6.9 million deaths as of March 2023. Cryo-EM (and cryo-ET) studies played a crucial role, in record time, in developing therapeutics targeted to the spike protein (S protein) that decorates the SARS-CoV-2 viral surface. Not only was the atomic structure of many S protein specimens established by SPA cryo-EM analysis, but also its multiple conformational states, essential for understanding its mechanism of action, as well as the spike complexes with the human angiotensin-converting enzyme-2 (ACE2) receptor and neutralizing antibodies [114]. Basic research on previous limited outbreaks of the closely similar coronaviruses SARS-CoV-1 (SARS-CoV) in 2002 and Middle Eastern respiratory syndrome coronavirus (MERS-CoV) in 2012, as well as accumulated experience with other emergent viral pandemics (HIV and influenza viruses), were also fundamental to the development of mRNA-based vaccines and effective antibody therapies [16, 17]. This rapid structural analysis of SARS-CoV-2 indicates that our global society is prepared to apply similar strategies to combat future emerging viruses.

The immature S protein is proteolyzed into two subunits, S1 and S2, which form a heterodimer, which in turn assembles into a trimer that results in the spike on the virion that coats the viral surface [115] (Fig. 12.4). The S trimeric protein is a metastable fusion nanomachine; in situ analysis of S trimers by cryo-ET/STA of intact virions showed that most spikes are in the prefusion conformation, with only 3% in the postfusion conformation [21, 116]. The receptor-binding domain (RBD), located in the S1 subunit, can be in a "down" or "up" conformation that corresponds to ACE2-inaccessible or -accessible conformations, respectively. During infection, RBD of the prefusion form in the up conformation binds to ACE2 before fusion of viral and host membrane, mediated by the fusion peptide in S2. The S protein, which elicits a strong immune response, is the most important target antigen for the development of therapeutics and current vaccines. The Moderna and Pfizer mRNA vaccines are based on S protein stabilized in the prefusion conformation by two-proline substitutions [117]. Neutralizing antibodies to specific S protein regions and recombinant ACE2-derived inhibitors are also promising therapeutic agents for treating emergent variants. Another ~25 proteins have been described; many of these, some still structurally uncharacterized, are under study as candidate targets for antiviral drug development [118].

Cryo-ET in the Study of Enveloped Viruses and the Viral Life Cycle in the Host

Cryo-ET has allowed 3D analysis of complex and/or pleomorphic enveloped viral particles in vitro, many of them responsible for human diseases such as

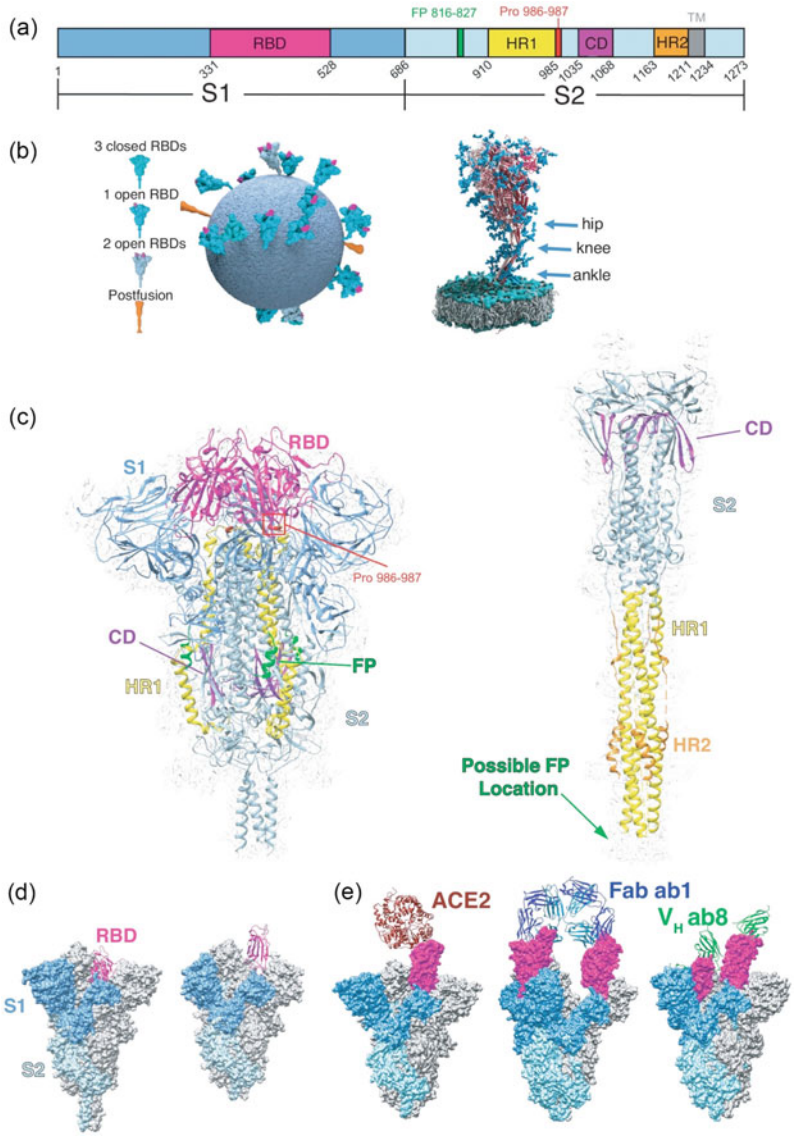

Fig. 12.4 Structures of SARS-CoV-2 spikes. **a** Scheme of the SARS-CoV-2 S domains showing the S1 subunit, S2 subunit, Receptor binding domain (RBD), fusion peptide (FP), heptad repeat 1 (HR1), connector domain (CD), heptad repeat 2 (HR2) and the transmembrane region (TM). **b** 3D model of a SARS-CoV-2 virion showing the conformations and flexibility of S on the virion surface. Three flexible hinges are marked by arrows (right). **c** SPA cryo-EM structure of the S trimer in its pre-fusion (left) and post-fusion (right) conformations [structural elements colored as in (**a**)]. **d** Comparison of S with RBD in the down (left) and up (right) conformations. **e** Cryo-EM structures of S bound to ACE2 with RBD in the up conformation (left), SN501Y mutant bound by Fab ab1 with RBD in the up conformation (middle), and SN501Y bound by VH ab8 in both the RBD up and down conformations (right). Reproduced with permission from Ref. [118]

HIV-1 [22, 119], herpesviruses [65, 120], and influenza virus [66, 121]. In addition, cryo-ET permits study of the viral replication cycle, including entry, replication, assembly, maturation, and egress within the native environment –the cell– at unprecedented resolution. STA typically improves resolution to ∼2–3 nm, and in some cases is able to achieve ∼4 Å resolution, that is, the cryo-ET resolution revolution [122]. We highlight a few examples for which cryo-ET has yielded important (and in some cases unanticipated) discoveries of complex viruses and in situ viral infection. The helical nucleocapsid (NC) of Ebola virus (with a non-segmented, negative-sense ssRNA) was solved by a subtomogram averaging at 6.6-Å resolution [123]; the NP carboxy-terminal extended α-helix is important for RNP assembly and recruitment of accessory proteins (Fig. 12.5a). In the study of HIV-1, a 7 Å resolution cryo-ET structure of the capsid from intact virions confirmed the hollow cone shape of the capsid, and allowed specific placement of each individual capsid hexamer and pentamer within the lattice structure [124]. The structure of the capsid domain and spacer peptide 1 (CA-SP1) of Gag (the precursor that includes MA, CA, and NC) in immature capsids was solved at 3.9-Å resolution [22], a value previously feasible only by single-particle cryo-EM. In influenza A virus (IAV), the matrix protein (M1) forms an endoskeleton beneath the virus membrane within intact virions. Cryo-ET/STA at ∼8 Å resolution of M1 within purified virus particles, as well as the structure of M1 oligomers reconstituted in vitro, offered insights into IAV assembly and disassembly [125].

Although the icosahedral viruses that infect Archaea belong to the HK97 and PRD1 lineages, other archaeal viruses, such as the bottle-, lemon- or spindle-shaped viruses, have unique morphologies and are optimal assemblies for study using cryo-ET [127]. Construction of tailed spindle viruses involves a metastable multistart helical assembly of variable width that extends through the lemon-shaped capsid and into the tail. These conformational capsid dynamics could be used to drive genome ejection into the host cell. Cryo-ET analysis of the nodavirus flock house virus, a positive ssRNA eukaryotic virus, has identified a genome-replication complex associated with membrane vesicles at 8.5 Å resolution by cryo-ET [126] (Fig. 12.5b) similar to that of many other (+) ssRNA viruses (including SARS-CoV-2) [128]. In the remodeled host membranes, these complexes resemble a crown (determined by STA), a dodecameric ring with RNA polymerase activity that gates release of progeny ssRNA molecules [129].

Cryogenic correlative light and electron microscopy (cryo-CLEM), which combines spatiotemporal information from fluorescence microscopy (proteins of interest are tagged with fluorescent labels) with structural data from cryo-ET, is very appropriate for studying viral assembly and/or infrequent and short-lived events in selected regions of virus-infected cells [130, 131]. *Pseudomonas* phages assemble a compartment for DNA replication. Before cell lysis to release phages, assembled empty capsids on the host cell membrane migrate along the PhuZ spindles to the compartment surface for DNA packaging before release of viral progeny [132, 133]. A phase plate cryo-ET study of cyanophage Syn5, which infects the cyanobacterium *Synechococcus*, identifies distinct assembly intermediates in situ such as procapsids with SP, expanded empty and full capsids, and complete virions with the tail [134].

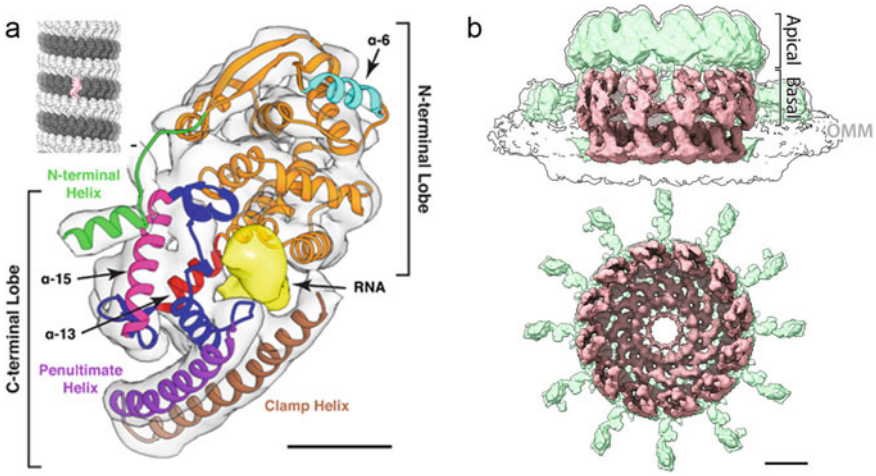

Fig. 12.5 Cryo-ET of pleomorphic viruses and intracellular viral assembly. **a** Structure of the helical nucleocapsid of Ebola virus solved by STA, indicating N- and C-terminal regions of nucleocapsid and the putative RNA density (yellow). Model of the helical RNP calculated by docking of NC in a tomogram (inset, a single NC is highlighted in pink). Scale bar, 20 Å. Adapted with permission from Ref. [123]. **b** The mature nodavirus crown resolved by cryo-ET STA comprises two stacked 12-mer rings (pink and green) of the viral RNA replication protein A. The lower ring, termed "proto-crown" (pink), is a precursor in RNA replication complex assembly, and protein A has alternate conformation in each ring. Reproduced with permission from Ref. [126]

In summary, advances in cryo-ET and associated techniques such as cryo-FIB milling have provided key insights that have expanded our knowledge of intracellular activities of viruses at unprecedented resolution.

Liquid Electron Microscopy (Liquid-EM)

Liquid electron microscopy (liquid-EM) is a relatively new technique that allows to image biological samples in their native liquid state. Unlike traditional transmission EM, which requires samples to be fixed (EM) or vitrified (cryo-EM) in a vacuum environment, liquid-EM delivers real-time data of dynamic processes in solution. Although liquid-EM results may not reach the resolution achieved with cryo-EM studies, it provides complementary information to cryo-EM/ET analyses [135]. Liquid-EM have been used to image multiple dynamic states of Adeno-associated virus in solution [136] and real-time host–pathogen interactions of phages with bacteria in solution [137].

Acknowledgements We apologize to our colleagues with outstanding contributions who were not mentioned due to space limitations. The authors thank C. Mark for editorial assistance. This work was supported by a grant of the Instituto de Salud Carlos III (PI20CIII-00014) to DL, and

by grants from the Spanish Ministry of Science and Innovation (PID2020-113287RB-I00) and the Comunidad Autónoma de Madrid (P2018/NMT- 4389) to JRC.

References

1. Schlicksup CJ et al (2018) Hepatitis B virus core protein allosteric modulators can distort and disrupt intact capsids. Elife 7. https://doi.org/10.7554/eLife.31473
2. Schwarz B, Uchida M, Douglas T (2017) Biomedical and catalytic opportunities of virus-like particles in nanotechnology. Adv Virus Res 97:1–60. https://doi.org/10.1016/bs.aivir.2016.09.002
3. Chua EYD et al (2022) Better, faster, cheaper: recent advances in cryo-electron microscopy. Annu Rev Biochem 91:1–32. https://doi.org/10.1146/annurev-biochem-032620-110705
4. Chmielewski D, Chiu W (2021) Encyclopedia of virology. In: Bamford DH, Zuckerman M 4th edn, vol. 1. Academic Press, pp 233–241
5. Bertozzi C (2017) Atoms out of blobs: CryoEM takes the nobel prize in chemistry. ACS Cent Sci 3:1056. https://doi.org/10.1021/acscentsci.7b00494
6. Cianfrocco MA, Kellogg EH (2020) What could go wrong? a practical guide to single-particle cryo-EM: from biochemistry to atomic models. J Chem Inf Model 60:2458–2469. https://doi.org/10.1021/acs.jcim.9b01178
7. Jiang W, Tang L (2017) Atomic cryo-EM structures of viruses. Curr Opin Struct Biol 46:122–129. https://doi.org/10.1016/j.sbi.2017.07.002
8. Kaelber JT, Hryc CF, Chiu W (2017) Electron cryomicroscopy of viruses at near-atomic resolutions. Annu Rev Virol 4:287–308. https://doi.org/10.1146/annurev-virology-101416-041921
9. Khoshouei M, Radjainia M, Baumeister W, Danev R (2017) Cryo-EM structure of haemoglobin at 3.2 A determined with the Volta phase plate. Nat Commun 8:16099. https://doi.org/10.1038/ncomms16099
10. Merk A et al (2016) Breaking cryo-EM resolution barriers to facilitate drug discovery. Cell 165:1698–1707. https://doi.org/10.1016/j.cell.2016.05.040
11. Lucic V, Rigort A, Baumeister W (2013) Cryo-electron tomography: the challenge of doing structural biology in situ. J Cell Biol 202:407–419. https://doi.org/10.1083/jcb.201304193
12. Wan W, Briggs JA (2016) Cryo-electron tomography and subtomogram averaging. Methods Enzymol 579:329–367. https://doi.org/10.1016/bs.mie.2016.04.014
13. Sirohi D et al (2016) The 3.8 A resolution cryo-EM structure of Zika virus. Science 352:467–470. https://doi.org/10.1126/science.aaf5316
14. Sugita Y, Matsunami H, Kawaoka Y, Noda T, Wolf M (2018) Cryo-EM structure of the Ebola virus nucleoprotein-RNA complex at 3.6 A resolution. Nature 563:137–140. https://doi.org/10.1038/s41586-018-0630-0
15. Zhang X et al (2013) Cryo-EM structure of the mature dengue virus at 3.5-A resolution. Nat Struct Mol Biol 20:105–110. https://doi.org/10.1038/nsmb.2463
16. Yuan Y et al (2017) Cryo-EM structures of MERS-CoV and SARS-CoV spike glycoproteins reveal the dynamic receptor binding domains. Nat Commun 8:15092. https://doi.org/10.1038/ncomms15092
17. Pallesen J et al (2017) Immunogenicity and structures of a rationally designed prefusion MERS-CoV spike antigen. Proc Natl Acad Sci U S A 114:E7348–E7357. https://doi.org/10.1073/pnas.1707304114
18. Nakane T et al (2020) Single-particle cryo-EM at atomic resolution. Nature 587:152–156. https://doi.org/10.1038/s41586-020-2829-0
19. Yip KM, Fischer N, Paknia E, Chari A, Stark H (2020) Atomic-resolution protein structure determination by cryo-EM. Nature 587:157–161. https://doi.org/10.1038/s41586-020-2833-4

20. Quemin ERJ et al (2020) Cellular electron cryo-tomography to study virus-host interactions. Annu Rev Virol 7:239–262. https://doi.org/10.1146/annurev-virology-021920-115935
21. Yao H et al (2020) Molecular architecture of the SARS-CoV-2 Virus. Cell. https://doi.org/10.1016/j.cell.2020.09.018
22. Schur FK et al (2016) An atomic model of HIV-1 capsid-SP1 reveals structures regulating assembly and maturation. Science 353:506–508. https://doi.org/10.1126/science.aaf9620
23. Kuhlbrandt W (2014) Biochemistry. The resolution revolution. Science 343:1443–1444. https://doi.org/10.1126/science.1251652
24. Nogales E, Scheres SH (2015) Cryo-EM: a unique tool for the visualization of macromolecular complexity. Mol Cell 58:677–689. https://doi.org/10.1016/j.molcel.2015.02.019
25. Elmlund D, Le SN, Elmlund H (2017) High-resolution cryo-EM: the nuts and bolts. Curr Opin Struct Biol 46:1–6. https://doi.org/10.1016/j.sbi.2017.03.003
26. Harris JR (1997) Negative staining and cryoelectron microscopy: the thin film techniques. BIOS Scientific Publishers Ltd.
27. Dubochet J et al (1988) Cryo-electron microscopy of vitrified specimens. Q Rev Biophys 21:129–228
28. Dobro MJ, Melanson LA, Jensen GJ, McDowall AW (2010) Plunge freezing for electron cryomicroscopy. Methods Enzymol 481:63–82. https://doi.org/10.1016/S0076-6879(10)81003-1
29. Grassucci RA, Taylor DJ, Frank J (2007) Preparation of macromolecular complexes for cryo-electron microscopy. Nat Protoc 2:3239–3246. https://doi.org/10.1038/nprot.2007.452
30. Henderson R (1992) Image contrast in high-resolution electron microscopy of biological macromolecules: TMV in ice. Ultramicroscopy 46:1–18
31. Conway JF et al (1993) The effects of radiation damage on the structure of frozen hydrated HSV-1 capsids. J Struct Biol 111:222–233. S1047-8477(83)71052-X [pii] https://doi.org/10.1006/jsbi.1993.1052
32. Bammes BE, Jakana J, Schmid MF, Chiu W (2010) Radiation damage effects at four specimen temperatures from 4 to 100 K. J Struct Biol 169:331–341. https://doi.org/10.1016/j.jsb.2009.11.001
33. D'Imprima E et al (2019) Protein denaturation at the air-water interface and how to prevent it. eLife 8. https://doi.org/10.7554/eLife.42747
34. Klebl DP et al (2020) Need for speed: examining protein behavior during CryoEM grid preparation at different timescales. Structure 28:1238–1248 e1234. https://doi.org/10.1016/j.str.2020.07.018
35. Wei H et al (2018) Optimizing "self-wicking" nanowire grids. J Struct Biol 202:170–174. https://doi.org/10.1016/j.jsb.2018.01.001
36. Schmidli C et al (2019) Microfluidic protein isolation and sample preparation for high-resolution cryo-EM. Proc Natl Acad Sci U S A 116:15007–15012. https://doi.org/10.1073/pnas.1907214116
37. Rubinstein JL et al (2019) Shake-it-off: a simple ultrasonic cryo-EM specimen-preparation device. Acta Crystallogr D Struct Biol 75:1063–1070. https://doi.org/10.1107/S2059798319014372
38. Ravelli RBG et al (2020) Cryo-EM structures from sub-nl volumes using pin-printing and jet vitrification. Nat Commun 11:2563. https://doi.org/10.1038/s41467-020-16392-5
39. Kontziampasis D et al (2019) A cryo-EM grid preparation device for time-resolved structural studies. IUCrJ 6:1024–1031. https://doi.org/10.1107/S2052252519011345
40. Passmore LA, Russo CJ (2016) Specimen preparation for high-resolution Cryo-EM. Methods Enzymol 579:51–86. https://doi.org/10.1016/bs.mie.2016.04.011
41. Duong-Ly KC, Gabelli SB (2014) Gel filtration chromatography (size exclusion chromatography) of proteins. Methods Enzymol 541:105–114. https://doi.org/10.1016/B978-0-12-420119-4.00009-4
42. Skiniotis G, Southworth DR (2016) Single-particle cryo-electron microscopy of macromolecular complexes. Microscopy (Oxf) 65:9–22. https://doi.org/10.1093/jmicro/dfv366

43. Kastner B et al (2008) GraFix: sample preparation for single-particle electron cryomicroscopy. Nat Methods 5:53–55. https://doi.org/10.1038/nmeth1139
44. McMullan G, Faruqi AR, Clare D, Henderson R (2014) Comparison of optimal performance at 300keV of three direct electron detectors for use in low dose electron microscopy. Ultramicroscopy 147:156–163. https://doi.org/10.1016/j.ultramic.2014.08.002
45. McMullan G, Faruqi AR, Henderson R (2016) Direct electron detectors. Methods Enzymol 579:1–17. https://doi.org/10.1016/bs.mie.2016.05.056
46. Brilot AF et al (2012) Beam-induced motion of vitrified specimen on holey carbon film. J Struct Biol 177:630–637. https://doi.org/10.1016/j.jsb.2012.02.003
47. Scheres SH (2014) Beam-induced motion correction for sub-megadalton cryo-EM particles. Elife 3:e03665. https://doi.org/10.7554/eLife.03665
48. Li X et al (2013) Electron counting and beam-induced motion correction enable near-atomic-resolution single-particle cryo-EM. Nat Methods 10:584–590. https://doi.org/10.1038/nmeth.2472
49. Grant T, Grigorieff N (2015) Measuring the optimal exposure for single particle cryo-EM using a 2.6 A reconstruction of rotavirus VP6. Elife 4:e06980. https://doi.org/10.7554/eLife.06980
50. Ripstein ZA, Rubinstein JL (2016) Processing of cryo-EM movie data. Methods Enzymol 579:103–124. https://doi.org/10.1016/bs.mie.2016.04.009
51. Russo CJ, Passmore LA (2014) Electron microscopy: ultrastable gold substrates for electron cryomicroscopy. Science 346:1377–1380. https://doi.org/10.1126/science.1259530
52. Naydenova K, Russo CJ (2022) Integrated wafer-scale manufacturing of electron cryomicroscopy specimen supports. Ultramicroscopy 232:113396. https://doi.org/10.1016/j.ultramic.2021.113396
53. Mastronarde DN (2005) Automated electron microscope tomography using robust prediction of specimen movements. J Struct Biol 152:36–51. https://doi.org/10.1016/j.jsb.2005.07.007
54. Cheng A et al (2021) Leginon: new features and applications. Protein Sci 30:136–150. https://doi.org/10.1002/pro.3967
55. Zhang J et al (2009) JADAS: a customizable automated data acquisition system and its application to ice-embedded single particles. J Struct Biol 165:1–9. https://doi.org/10.1016/j.jsb.2008.09.006
56. Cheng Y, Grigorieff N, Penczek PA, Walz T (2015) A primer to single-particle cryo-electron microscopy. Cell 161:438–449. https://doi.org/10.1016/j.cell.2015.03.050
57. Scheres SH (2016) Processing of structurally heterogeneous cryo-EM Data in Relion. Methods Enzymol 579:125–157. https://doi.org/10.1016/bs.mie.2016.04.012
58. Ludtke SJ (2016) Single-particle refinement and variability analysis in EMAN2.1. Methods Enzymol 579:159–189. https://doi.org/10.1016/bs.mie.2016.05.001
59. Punjani A, Rubinstein JL, Fleet DJ, Brubaker MA (2017) cryoSPARC: algorithms for rapid unsupervised cryo-EM structure determination. Nat Methods 14:290–296. https://doi.org/10.1038/nmeth.4169
60. Grigorieff N (2016) Frealign: an exploratory tool for single-particle Cryo-EM. Methods Enzymol 579:191–226. https://doi.org/10.1016/bs.mie.2016.04.013
61. de la Rosa-Trevin JM et al (2016) Scipion: a software framework toward integration, reproducibility and validation in 3D electron microscopy. J Struct Biol 195:93–99. https://doi.org/10.1016/j.jsb.2016.04.010
62. Scheres SH (2012) RELION: implementation of a Bayesian approach to cryo-EM structure determination. J Struct Biol 180:519–530. https://doi.org/10.1016/j.jsb.2012.09.006
63. Scheres SH et al (2007) Disentangling conformational states of macromolecules in 3D-EM through likelihood optimization. Nat Methods 4:27–29. https://doi.org/10.1038/nmeth992
64. Lyumkis D, Brilot AF, Theobald DL, Grigorieff N (2013) Likelihood-based classification of cryo-EM images using FREALIGN. J Struct Biol 183:377–388. https://doi.org/10.1016/j.jsb.2013.07.005
65. Goetschius DJ, Lee H, Hafenstein S (2019) CryoEM reconstruction approaches to resolve asymmetric features. Adv Virus Res 105:73–91. https://doi.org/10.1016/bs.aivir.2019.07.007

66. Huiskonen JT (2018) Image processing for cryogenic transmission electron microscopy of symmetry-mismatched complexes. Biosci Rep 38. https://doi.org/10.1042/BSR20170203
67. Penczek PA (2010) Fundamentals of three-dimensional reconstruction from projections. Methods Enzymol 482:1–33. https://doi.org/10.1016/S0076-6879(10)82001-4
68. Henderson R et al (2012) Outcome of the first electron microscopy validation task force meeting. Structure 20:205–214. https://doi.org/10.1016/j.str.2011.12.014
69. Scheres SH, Chen S (2012) Prevention of overfitting in cryo-EM structure determination. Nat Methods 9:853–854. https://doi.org/10.1038/nmeth.2115
70. Subramaniam S, Earl LA, Falconieri V, Milne JL, Egelman EH (2016) Resolution advances in cryo-EM enable application to drug discovery. Curr Opin Struct Biol 41:194–202. https://doi.org/10.1016/j.sbi.2016.07.009
71. Kucukelbir A, Sigworth FJ, Tagare HD (2014) Quantifying the local resolution of cryo-EM density maps. Nat Methods 11:63–65. https://doi.org/10.1038/nmeth.2727
72. Vilas JL et al (2018) MonoRes: automatic and accurate estimation of local resolution for electron microscopy maps. Structure 26:337–344 e334 (2018). https://doi.org/10.1016/j.str.2017.12.018
73. Luque D et al (2023) Equilibrium dynamics of a biomolecular complex analyzed at single-amino acid resolution by cryo-electron microscopy. J Mol Biol 435:168024. https://doi.org/10.1016/j.jmb.2023.168024
74. Burnley T, Palmer CM, Winn M (2017) Recent developments in the CCP-EM software suite. Acta Crystallogr D Struct Biol 73:469–477. https://doi.org/10.1107/S2059798317007859
75. Afonine PV et al (2018) Real-space refinement in PHENIX for cryo-EM and crystallography. Acta Crystallogr D Struct Biol 74:531–544. https://doi.org/10.1107/S2059798318006551
76. Wang RY et al (2016) Automated structure refinement of macromolecular assemblies from cryo-EM maps using Rosetta. eLife 5. https://doi.org/10.7554/eLife.17219
77. Pettersen EF et al (2021) UCSF ChimeraX: structure visualization for researchers, educators, and developers. Protein Sci 30:70–82. https://doi.org/10.1002/pro.3943
78. Croll TI (2018) ISOLDE: a physically realistic environment for model building into low-resolution electron-density maps. Acta Crystallogr D Struct Biol 74:519–530. https://doi.org/10.1107/S2059798318002425
79. Casanal A, Lohkamp B, Emsley P (2020) Current developments in Coot for macromolecular model building of Electron Cryo-microscopy and crystallographic data. Protein Sci 29:1069–1078. https://doi.org/10.1002/pro.3791
80. Jumper J et al (2021) Highly accurate protein structure prediction with AlphaFold. Nature 596:583–589. https://doi.org/10.1038/s41586-021-03819-2
81. Baek M et al (2021) Accurate prediction of protein structures and interactions using a three-track neural network. Science 373:871–876. https://doi.org/10.1126/science.abj8754
82. Zhang P, Mendonça L (2021) Encyclopedia of virology. In: Bamford DH, Zuckerman M (eds) 4th edn. vol. 1, Academic Press, pp 242–247
83. Schaffer M et al (2017) Optimized cryo-focused ion beam sample preparation aimed at in situ structural studies of membrane proteins. J Struct Biol 197:73–82. https://doi.org/10.1016/j.jsb.2016.07.010
84. Oikonomou CM, Jensen GJ (2017) Cellular electron cryotomography: toward structural biology in situ. Annu Rev Biochem 86:873–896. https://doi.org/10.1146/annurev-biochem-061516-044741
85. Turk M, Baumeister W (2020) The promise and the challenges of cryo-electron tomography. FEBS Lett 594:3243–3261. https://doi.org/10.1002/1873-3468.13948
86. Stass R, Ilca SL, Huiskonen JT (2018) Beyond structures of highly symmetric purified viral capsids by cryo-EM. Curr Opin Struct Biol 52:25–31. https://doi.org/10.1016/j.sbi.2018.07.011
87. Jose J, Hafenstein SL (2022) Asymmetry in icosahedral viruses. Curr Opin Virol 54:101230. https://doi.org/10.1016/j.coviro.2022.101230
88. Twarock R, Bingham RJ, Dykeman EC, Stockley PG (2018) A modelling paradigm for RNA virus assembly. Curr Opin Virol 31:74–81. https://doi.org/10.1016/j.coviro.2018.07.003

89. Twarock R, Stockley PG (2019) RNA-mediated virus assembly: mechanisms and consequences for viral evolution and therapy. Annu Rev Biophys 48:495–514. https://doi.org/10.1146/annurev-biophys-052118-115611
90. Dai X et al (2017) In situ structures of the genome and genome-delivery apparatus in a single-stranded RNA virus. Nature 541:112–116. https://doi.org/10.1038/nature20589
91. Koning RI et al (2016) Asymmetric cryo-EM reconstruction of phage MS2 reveals genome structure in situ. Nat Commun 7:12524. https://doi.org/10.1038/ncomms12524
92. Gorzelnik KV et al (2016) Asymmetric cryo-EM structure of the canonical Allolevivirus Qbeta reveals a single maturation protein and the genomic ssRNA in situ. Proc Natl Acad Sci U S A 113:11519–11524. https://doi.org/10.1073/pnas.1609482113
93. Zhang X et al (2015) In situ structures of the segmented genome and RNA polymerase complex inside a dsRNA virus. Nature 527:531–534. https://doi.org/10.1038/nature15767
94. Liu YT, Jih J, Dai X, Bi GQ, Zhou ZH (2019) Cryo-EM structures of herpes simplex virus type 1 portal vertex and packaged genome. Nature 570:257–261. https://doi.org/10.1038/s41586-019-1248-6
95. Conley MJ et al (2019) Calicivirus VP2 forms a portal-like assembly following receptor engagement. Nature 565:377–381. https://doi.org/10.1038/s41586-018-0852-1
96. Liu H, Cheng L (2015) Cryo-EM shows the polymerase structures and a nonspooled genome within a dsRNA virus. Science 349:1347–1350.
97. Pan M, Alvarez-Cabrera AL, Kang JS, Wang L, Fan C, Zhou ZH (2021) Asymmetric reconstruction of mammalian reovirus reveals interactions among RNA, transcriptional factor micro2 and capsid proteins. Nat Commun 12:4176.
98. Ding K, Celma CC, Zhang X, Chang T, Shen W, Atanasov I, Roy P, Zhou ZH (2019) In situ structures of rotavirus polymerase in action and mechanism of mRNA transcription and release. Nat Commun 10: 2216.
99. Cui Y, Zhang Y, Zhou K, Sun J, Zhou ZH (2019) Conservative transcription in three steps visualized in a double-stranded RNA virus. Nat Struct Mol Biol 26:1023–1034.
100. He Y, Shivakoti S, Ding K, Cui Y, Roy P, Zhou ZH (2019) In situ structures of RNA-dependent RNA polymerase inside bluetongue virus before and after uncoating. Proc Natl Acad Sci 116:16535–16540.
101. Ilca SL et al (2019) Multiple liquid crystalline geometries of highly compacted nucleic acid in a dsRNA virus. Nature 570:252–256. https://doi.org/10.1038/s41586-019-1229-9
102. Li Z, Pang J, Dong L, Yu X (2021) Structural basis for genome packaging, retention, and ejection in human cytomegalovirus. Nat Commun 12:4538. https://doi.org/10.1038/s41467-021-24820-3
103. Abergel C, Legendre M, Claverie JM (2015) The rapidly expanding universe of giant viruses: Mimivirus, Pandoravirus Pithovirus and Mollivirus. FEMS Microbiol Rev 39:779–796. https://doi.org/10.1093/femsre/fuv037
104. Burton-Smith RN, Murata K (2021) Cryo-electron microscopy of the giant viruses. Microscopy (Oxf) 70:477–486. https://doi.org/10.1093/jmicro/dfab036
105. Chihara A et al (2022) A novel capsid protein network allows the characteristic internal membrane structure of Marseilleviridae giant viruses. Sci Rep 12:21428. https://doi.org/10.1038/s41598-022-24651-2
106. Zhu D et al (2018) Pushing the resolution limit by correcting the Ewald sphere effect in single-particle Cryo-EM reconstructions. Nat Commun 9:1552. https://doi.org/10.1038/s41467-018-04051-9
107. Downing KH, Glaeser RM (2018) Estimating the effect of finite depth of field in single-particle cryo-EM. Ultramicroscopy 184:94–99. https://doi.org/10.1016/j.ultramic.2017.08.007
108. Fang Q et al (2019) Near-atomic structure of a giant virus. Nat Commun 10:388. https://doi.org/10.1038/s41467-019-08319-6
109. Zhang X et al (2011) Three-dimensional structure and function of the Paramecium bursaria chlorella virus capsid. Proc Natl Acad Sci U S A 108:14837–14842. https://doi.org/10.1073/pnas.1107847108

110. Liu S et al (2019) Cryo-EM structure of the african swine fever virus. Cell Host Microbe 26:836–843 e833. https://doi.org/10.1016/j.chom.2019.11.004
111. Wang N et al (2019) Architecture of African swine fever virus and implications for viral assembly. Science 366:640–644. https://doi.org/10.1126/science.aaz1439
112. Pintilie G et al (2019) Segmentation and comparative modeling in an 8.6-A Cryo-EM map of the Singapore grouper iridovirus. Structure 27:1561–1569 e1564 (2019). https://doi.org/10.1016/j.str.2019.08.002
113. Benson SD, Bamford JK, Bamford DH, Burnett RM (2004) Does common architecture reveal a viral lineage spanning all three domains of life? Mol Cell 16:673–685. S1097276504007099 [pii] https://doi.org/10.1016/j.molcel.2004.11.016
114. Rapp M, Shapiro L, Frank J (2022) Contributions of single-particle cryoelectron microscopy toward fighting COVID-19. Trends Biochem Sci 47:117–123. https://doi.org/10.1016/j.tibs.2021.10.005
115. Cai Y et al (2020) Distinct conformational states of SARS-CoV-2 spike protein. Science 369:1586–1592. https://doi.org/10.1126/science.abd4251
116. Ke Z et al (2020) Structures and distributions of SARS-CoV-2 spike proteins on intact virions. Nature 588:498–502. https://doi.org/10.1038/s41586-020-2665-2
117. Wrapp D et al (2020) Cryo-EM Structure of the 2019-nCoV spike in the prefusion conformation. bioRxiv. https://doi.org/10.1101/2020.02.11.944462
118. Hardenbrook NJ, Zhang P (2022) A structural view of the SARS-CoV-2 virus and its assembly. Curr Opin Virol 52:123–134. https://doi.org/10.1016/j.coviro.2021.11.011
119. Vankadari N, Shepherd DC, Carter SD, Ghosal D (2022) Three-dimensional insights into human enveloped viruses in vitro and in situ. Biochem Soc Trans 50:95–105. https://doi.org/10.1042/BST20210433
120. Zeev-Ben-Mordehai T et al (2016) Two distinct trimeric conformations of natively membrane-anchored full-length herpes simplex virus 1 glycoprotein B. Proc Natl Acad Sci U S A 113:4176–4181. https://doi.org/10.1073/pnas.1523234113
121. Arranz R et al (2012) The structure of native influenza virion ribonucleoproteins. Science 338:1634–1637. https://doi.org/10.1126/science.1228172
122. Hong Y, Song Y, Zhang Z, Li S (2023) Cryo-electron tomography: the resolution revolution and a surge of in situ virological discoveries. Annu Rev Biophys. https://doi.org/10.1146/annurev-biophys-092022-100958
123. Wan W et al (2017) Structure and assembly of the Ebola virus nucleocapsid. Nature 551:394–397. https://doi.org/10.1038/nature24490
124. Mattei S, Glass B, Hagen WJ, Krausslich HG, Briggs JA (2016) The structure and flexibility of conical HIV-1 capsids determined within intact virions. Science 354:1434–1437. https://doi.org/10.1126/science.aah4972
125. Peukes J et al (2020) The native structure of the assembled matrix protein 1 of influenza a virus. Nature 587:495–498. https://doi.org/10.1038/s41586-020-2696-8
126. Zhan H et al (2023) Nodavirus RNA replication crown architecture reveals proto-crown precursor and viral protein a conformational switching. Proc Natl Acad Sci U S A 120:e2217412120. https://doi.org/10.1073/pnas.2217412120
127. Hochstein R et al (2018) Structural studies of Acidianus tailed spindle virus reveal a structural paradigm used in the assembly of spindle-shaped viruses. Proc Natl Acad Sci U S A 115:2120–2125. https://doi.org/10.1073/pnas.1719180115
128. Wolff G et al (2020) A molecular pore spans the double membrane of the coronavirus replication organelle. Science 369:1395–1398. https://doi.org/10.1126/science.abd3629
129. Unchwaniwala N, Zhan H, den Boon JA, Ahlquist P (2021) Cryo-electron microscopy of nodavirus RNA replication organelles illuminates positive-strand RNA virus genome replication. Curr Opin Virol 51:74–79. https://doi.org/10.1016/j.coviro.2021.09.008
130. Hampton CM et al (2017) Correlated fluorescence microscopy and cryo-electron tomography of virus-infected or transfected mammalian cells. Nat Protoc 12:150–167. https://doi.org/10.1038/nprot.2016.168
131. Chaikeeratisak V et al (2017) Assembly of a nucleus-like structure during viral replication in bacteria. Science 355:194–197. https://doi.org/10.1126/science.aal2130

132. Chaikeeratisak V et al (2019) Viral capsid trafficking along treadmilling tubulin filaments in Bacteria. Cell 177:1771–1780 e1712 (2019). https://doi.org/10.1016/j.cell.2019.05.032
133. Chaikeeratisak V et al (2017) The phage nucleus and tubulin spindle are conserved among large pseudomonas phages. Cell Rep 20:1563–1571. https://doi.org/10.1016/j.celrep.2017.07.064
134. Dai W et al (2013) Visualizing virus assembly intermediates inside marine cyanobacteria. Nature 502:707–710. https://doi.org/10.1038/nature12604
135. Kelly DF et al (2022) Liquid-EM goes viral - visualizing structure and dynamics. Curr Opin Struct Biol 75:102426. https://doi.org/10.1016/j.sbi.2022.102426
136. Jonaid GM et al (2021) High-resolution imaging of human viruses in liquid droplets. Adv Mater 33:e2103221. https://doi.org/10.1002/adma.202103221
137. Kennedy E, Nelson EM, Tanaka T, Damiano J, Timp G (2016) Live Bacterial physiology visualized with 5 nm resolution using scanning transmission electron microscopy. ACS Nano 10:2669–2677. https://doi.org/10.1021/acsnano.5b07697